Bulletin of the Seismological Society of America, Vol. 87, No. 4, pp. 1011–1023, August 1997

The 1978 Brooks Peninsula, Vancouver Island Earthquakes

by Chris Spindler, Garry C. Rogers, and John F. Cassidy

Abstract A pair of $M_W = 5.5$ earthquakes occurred beneath the Brooks Peninsula on the northwest coast of Vancouver Island on 2 June and 25 July 1978. These are the largest and best-recorded earthquakes to date in the vicinity of northern Vancouver Island and the adjacent coast margin. A detailed study of these earthquakes was undertaken to examine the contemporary tectonics of this region, specifically the poorly understood interaction between the Explorer plate and the North American plate at the northern end of the Cascadia subduction zone. Both earthquakes were followed by well-defined aftershock sequences. A four-station temporary seismograph array deployed on the Brooks Peninsula following the 2 June mainshock allowed for accurate aftershock locations. This earthquake was located at 50.15° N, 127.84° W, based on the center of a 9-km-diameter circular region of aftershocks. The 25 July earthquake was located 4 to 7 km to the northeast of the June epicenter based on waveform comparison of the two events. Both earthquakes occurred at 15 to 16 km depth. The focal mechanisms as determined from body-wave modeling are nearly identical and show left-lateral strike-slip motion along a shallow north-dipping, east–west-striking fault. The focal mechanism and depth of these two earthquakes indicates that they were not megathrust events on the Explorer/North America plate boundary, but rather that they occurred within the North American plate, 5 to 10 km above the megathrust. The northeast-directed pressure axes for these earthquakes suggests coupling across the Explorer–North America segment of the Cascadia subduction zone, consistent with contemporary convergence of the Explorer Plate with the North American plate in a northeast–southwest direction.

Introduction

In the summer of 1978, two significant earthquakes occurred on the Brooks Peninsula, on the west coast of Vancouver Island. The first earthquake, on 2 June, had magnitudes of $m_b = 5.0$, $M_S = 5.2$, and $M_W = 5.5$, and the second, on 25 July, magnitudes of $m_b = 5.2$, $M_S = 5.1$, and $M_W = 5.5$. These earthquakes were felt throughout northern Vancouver Island to a distance of 200 km (Horner *et al.*, 1979). The maximum felt intensity was V, and there was slight damage in Port Alice (about 30 km to the northeast of the epicenter—see Fig. 1) that was attributed to the June earthquake. Both events were followed by aftershock sequences. These were the largest earthquakes to have occurred on northern Vancouver Island since 1927, when one of similar size occurred in the same region.

As the largest, and best recorded earthquakes in the vicinity of the megathrust at the northern end of the Cascadia subduction zone to date, they provide an excellent opportunity to examine the contemporary tectonics of the region, specifically the poorly understood interaction between the Explorer and North America plates. They may also provide insight into the environment in the vicinity of the megathrust at other places along the Cascadia subduction zone. The deployment of portable seismographs to study the aftershock sequence of the 2 June earthquake provided the most accurate hypocenter locations of any yet determined in this area, and the nearby location of a marine seismic reflection line (Fig. 1) permits the hypocenters to be accurately positioned relative to local structure.

The source parameters of these earthquakes (location, depth, magnitude, seismic moment, and focal mechanism) were determined using local, regional, and teleseismic arrival-time data; the aftershock data; first-motion polarities; body-wave modeling; and far-field displacement spectra.

Tectonic Setting of Vancouver Island

Vancouver Island lies above the northern portion of the Cascadia subduction zone. Here, the Juan de Fuca and Explorer plates lie between the much larger Pacific and North America plates (Fig. 1). Beneath southern and central Vancouver Island (south of the Nootka fault zone—see Fig. 1), the Juan de Fuca plate is subducting beneath the North American plate with a convergence rate of 47 mm/yr in the direction N56°E. However, beneath northern Vancouver Island (i.e., north of the Nootka fault zone), the Explorer plate

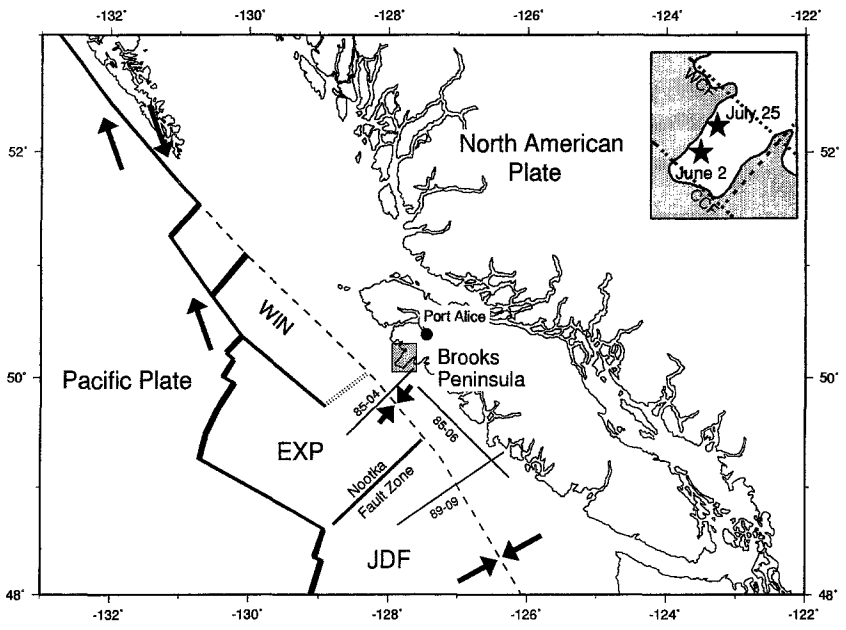

Figure 1. Tectonic setting of the Vancouver Island region. Arrows indicate the direction and velocity of the relative plate motions. EXP represents the Explorer plate, JDF is the Juan de Fuca plate, and WIN is the Winona block. The dashed line represents the convergent margin. The 2 June 1978 and 25 July 1978 earthquakes occurred beneath the Brooks Peninsula (inset). The major faults in the vicinity of the peninsula are shown in the inset; CCF and WCF denote the Cape Cook Fault and the Westcoast fault, respectively. Numbered lines are seismic reflection lines.

may have stopped subducting in an absolute sense, but it is still being overridden by the North American plate that is moving at the rate of about 20 mm/yr in the direction S50°W in the region of the Brooks Peninsula (Riddihough, 1984). Several seismic reflection lines (85-04, 85-06, and 89-09—see Fig. 1) provide constraints on the subduction structure of the region. Seismic data from line 85-04 (only 10 to 15 km from the epicenters of the 1978 earthquakes) show that the top of the Explorer plate is at 22 to 24 km depth (with an uncertainty of 1 to 2 km) in the vicinity of the Brooks Peninsula (Clowes *et al.*, 1997).

North of the Brooks Peninsula, the northernmost portion of the Explorer plate, the Winona Block (Fig. 1), may be acting independently as it converges with the North American plate (Davis and Riddihough, 1982). For details of the tectonics and contemporary motions of the plates in this region (based largely on seafloor magnetic anomaly data and rigid-plate analysis), see Riddihough (1977, 1984), Botros and Johnson (1988), Riddihough and Hyndman (1991), and Davis and Currie (1993).

Geology and Structure of the Brooks Peninsula

The Brooks Peninsula is located on the west coast of the northern end of Vancouver Island and covers an area of roughly 170 km^2 (Fig. 1). It is inaccessible by land and uninhabited. Due to the dense vegetation and difficult terrain, detailed geological surveys have been impossible. However, reconnaissance of the bedrock geology (Muller *et al.*, 1974; Smyth, 1985) has provided an overview of the geology and structure of the region. The peninsula is an uplifted block bounded on three sides by identified faults (Fig. 1 inset), and likely on the fourth as well, but no fault has been identified on the northwest coast. It is comprised of the Westcoast complex, derived from basic volcanic and intrusive rocks, metamorphosed in early Jurassic time. The Westcoast fault at the landward end of the peninsula separates the Westcoast complex from the main Wrangellia rocks of most of northern Vancouver Island. The Cape Cook fault at the southwest end of the peninsula separates the Westcoast complex from the Pacific Rim complex (Muller *et al.*, 1974), a melange unit that forms the southwestern tip of the peninsula (Smyth, 1985) and is presumably underthrust beneath it. Where the fault is exposed at the surface, it dips steeply to the northeast. The faults bounding the peninsula are similar to the general fault pattern on northern Vancouver Island in which the dominant faults strike northwest, dipping steeply to the northeast and are crosscut by steeply dipping, northeast-striking faults (Muller *et al.*, 1974). In the region of Brooks Peninsula, northeast-tending faults dominate and clearly cut the northwest-trending faults.

The Brooks Peninsula occupies a unique position on the western North American margin because the ridge–transform–trench triple junction between the Juan de Fuca, North American, and Pacific plates has been located off the peninsula for most of the past 10 m.y. (Riddihough, 1977) and perhaps longer (Wilson, 1988). The ridge intersection with the continental margin at Brooks Peninsula ended about 2 m.y.a. (Davis and Riddihough, 1982), but this location adjacent to the spreading ridge probably gave rise to the uplifted nature of the peninsula. It is perhaps significant that the contemporary interaction of the Chile Rise spreading ridge with the subduction margin in southern Chile has produced a similar uplifted block on the continental margin at 47° S, the Taito Peninsula (Forsythe and Nelson, 1985; Cande and Leslie, 1986). The Brooks Peninsula also marks the position of major tectonic boundary on Vancouver Island because for most of the past 10 m.y., subduction has been occurring south of the peninsula and not to the north. In the vicinity of the Winona Block just to the north of the Brooks Peninsula (Fig. 1), convergence with North America is re-

flected in offshore compressional features such as the Paul Revere Ridge (Davis and Riddihough, 1982), and it is not clear if any oceanic material has been forced beneath the continent in the past 2 m.y. since the triple junction migrated from its position off the Brooks Peninsula. The present-day heat flow signature reflects this as it drops to typically low values associated with the forearc of an active subduction zone as a line extending inland from the peninsula is crossed from north to south. Major geochemical, geophysical, and physiographic changes also occur as this line is crossed (Lewis *et al.*, 1997; Ellis *et al.*, 1996).

The Brooks Peninsula is also reflected in the seismicity pattern. The Nootka fault zone, the boundary between the Explorer and Juan de Fuca plates, is the broadband of seismicity perpendicular to Vancouver Island that dominates the seismicity pattern (Fig. 2), but there is a noticeable concentration of seismic activity on the continental slope and shelf adjacent to the Brooks Peninsula. The point to make is that earthquakes along the Nootka fault zone, and almost all the other seismicity beneath the continental shelf, occurs within the subducted oceanic plate. We will show that the two 1978 events are in the overlying North American plate, and by association, the concentration of seismicity near the Brooks Peninsula shown in Fig. 2 is also inferred to be in the overlying plate. The occurrence of earthquakes of the size of the 1978 events within the overlying North American plate so close to the megathrust (i.e., within tens of kilometers) is unique along the whole Cascadia subducting margin north of the intense activity in the Cape Mendicino triple junction region of northern California (e.g., Smith *et al.*, 1993; Wang and Rogers, 1994) where the large (M_W = 7.2) Petrolia earthquake occurred in 1992 (Oppenheimer *et al.*, 1993; Velasco *et al.*, 1994; Tinker and Beck, 1995). In the vicinity of the northern Cascadia subduction zone, no underthrusting events have been detected on the plate boundary (Rogers, 1988). However, there is ample evidence for large, periodic subduction earthquakes along the Cascadia margin (for a summary, see Atwater *et al.*, 1995).

Results

Mainshock Locations

In this study, the two mainshocks were located using regional, teleseismic, and aftershock data. Due to the sparse regional data set, and the large inherent uncertainties in teleseismic solutions, our preferred epicenter for the June earthquake (Table 1) was chosen as the center of the circular distribution of well-located aftershocks recorded by a temporary array (described later in this article). Our preferred epicenter for the July event (Table 1) is based on a waveform comparison of the two earthquakes, yielding an accurate location relative to that of the June event.

Regional Locations. The initial solutions determined by the Geological Survey of Canada from regional observations and routine processing (Horner *et al.*, 1979) yielded locations (Fig. 3) of 50.13° N, 127.64° W for the June event (M_L = 5.7), and 50.19° N, 127.37° W for the July event (M_L = 5.6). These solutions are 15 to 30 km to the east of the well-located aftershocks on the northwest coast of the Brooks Peninsula. However, the regional epicenters are subject to significant uncertainties because of the following factors: all of the seismic stations used are located to one side of the earthquake (Fig. 3 inset), there were only two stations within 150 km of the epicenter, and the *S* arrivals were clipped and too faint to be read at the closest stations.

Teleseismic Locations. Teleseismic *P* arrival times were also used to estimate the locations of the two events. The

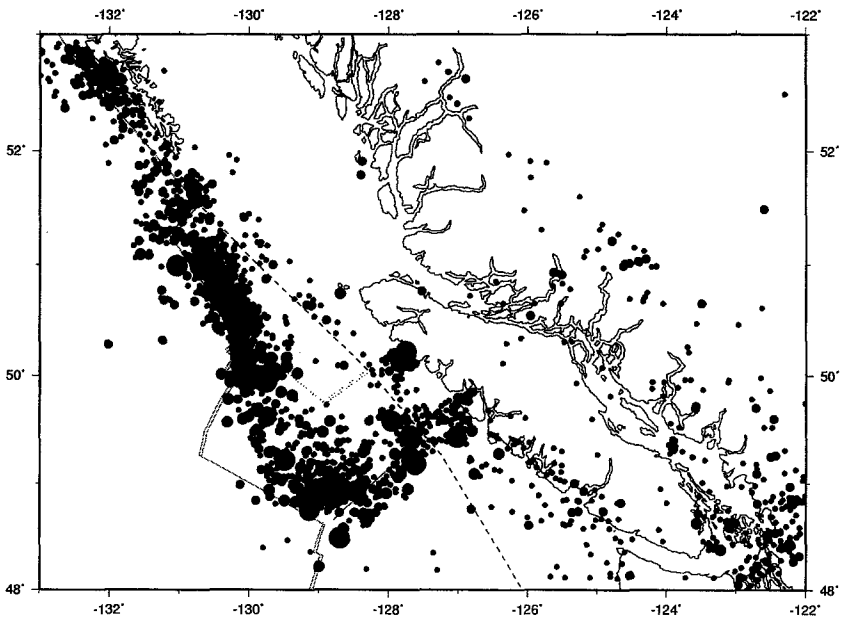

Figure 2. Seismicity of the Vancouver Island region 1978 to 1991 (from the Canadian Earthquake Epicenter File). The filled dots represent epicenters; their radius is scaled to the magnitude, from M = 2 to M = 6. With the exception of the triple junction regions and the Nootka fault zone, the 1978 Brooks Peninsula earthquakes represent the two largest earthquakes recorded to date near the continental slope along the Cascadia margin.

Table 1
Summary of Source Parameters

Parameter	2 June 1978	25 July 1978	Comments
Origin time	20:41:45 UTC	23:30:55 UTC	GSC
Location	50.15° N (±3.5 km) 127.84° W (±3.5 km)	50.19° N (±4.5 km) 127.79° W (±4.5 km)	based on center of aftershocks
Focal depth	15.0 ± 2 km	16.0 ± 2 km	
m_b	5.0 (72 obs.)	5.2 (81 obs.)	ISC
M_S	5.2 (24 obs.)	5.1 (20 obs.)	ISC
M_0	$(1.8 \pm 0.4) \times 10^{24}$ dyne-cm	$(1.7 \pm 0.4) \times 10^{24}$ dyne-cm	
M_W	5.5 (17 obs.)	5.5 (17 obs.)	
Stress drop	16–20 bars	16–18 bars	
Focal mechanism	267/25/0 (strike/dip/slip)	267/40/0 (strike/dip/slip)	
Pressure axis	244°/40° (strike/plunge)	234°/33° (strike/plunge)	
Tension axis	110°/40° (strike/plunge)	120°/33° (strike/plunge)	
Rupture area	40 km^2	38 km^2	

program EPDET (Weichert and Newton, 1970) was used along with the Jeffreys–Bullen earth model to locate the mainshock epicenters. The focal depth of the June event was fixed at 17 km on the basis of the aftershock study. Epicentral solutions determined using all of the available *P* arrival times from the International Seismological Centre (ISC) bulletin (219 for the June event and 204 for the July event) placed the events approximately 15 km to the northeast of the aftershocks (Fig. 3). To eliminate the effects of inhomogeneities in the crust and upper mantle, calculations using only those stations at epicentral distances greater than 20° were used. This reduced the June data set to 173 observations and the July data set to 167 observations. Further, stations having large travel-time residuals (greater than 4 sec) were removed from the solutions. The resulting epicenters (Fig. 3) were coincident within the location uncertainties and were within 5 km of the aftershocks. Different earth models and data subsets were tried (Spindler, 1991), and in all cases, the July epicenter was located 6 to 13 km to the east of the June event.

Body Waveform Comparisons. The location of the July event, relative to the June event, was accurately determined by comparing waveforms at seismograph stations to the north of the epicenter and to the east of the epicenter. Short-period recordings of the two events made at Inuvik, Northwest Territories (INK), to the north of the epicenter (azimuth = 353°, Δ = 18°), are nearly identical (Fig. 4a). Aligning these seismograms on the *SH* waves reveals that the July *Lg* wave train arrives 0.3 to 0.5 sec early relative to that of the June event (Fig. 4a). This requires the July epicenter to be located 3 to 5 km to the north of the June epicenter. To constrain the location in the E–W direction, the long-period vertical-component recordings of the two events at Ottawa (OTT), Ontario (azimuth = 77°, Δ = 35°), are compared in Figure 4b. Aligning these seismograms on the *P* waveforms shows that the Rayleigh waves of the July earthquake arrive 0.8 to 1.2 sec early relative to those of the June event. This indicates that the July epicenter is between 4 and 6 km to the east of the June epicenter. Combining these two results indicates that the July event was 4 to 7 km to the NE of the June epicenter. Although not shown here, a comparison of the short-period waveforms at Fort Churchill, Manitoba (FCC), located to the northeast (azimuth = 53°, Δ = 21°), yields the same result; the July epicenter is 4 to 7 km to the NE of the June event.

Focal Depth

The focal depths of these earthquakes were well constrained by modeling long- and short-period teleseismic

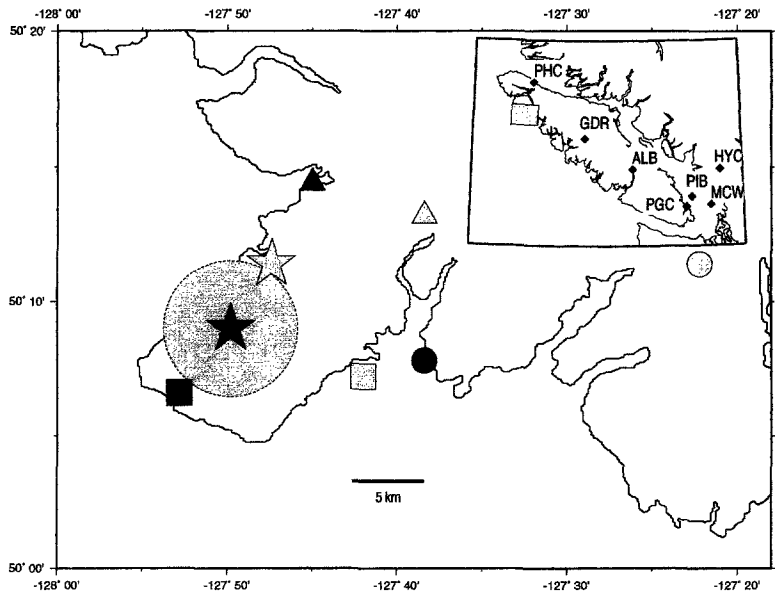

Figure 3. Epicentral estimates for the 2 June (solid symbols) and 25 July (shaded symbols) Brooks Peninsula earthquakes. Stars denote the preferred locations (see text); circles are the regional solutions from routine GSC processing, obtained using the stations shown in the inset; triangles are the teleseismic solutions obtained using all available data; and squares are the teleseismic solutions obtained using a refined data set (see text). The shaded circular region denotes the region of well-located aftershocks.

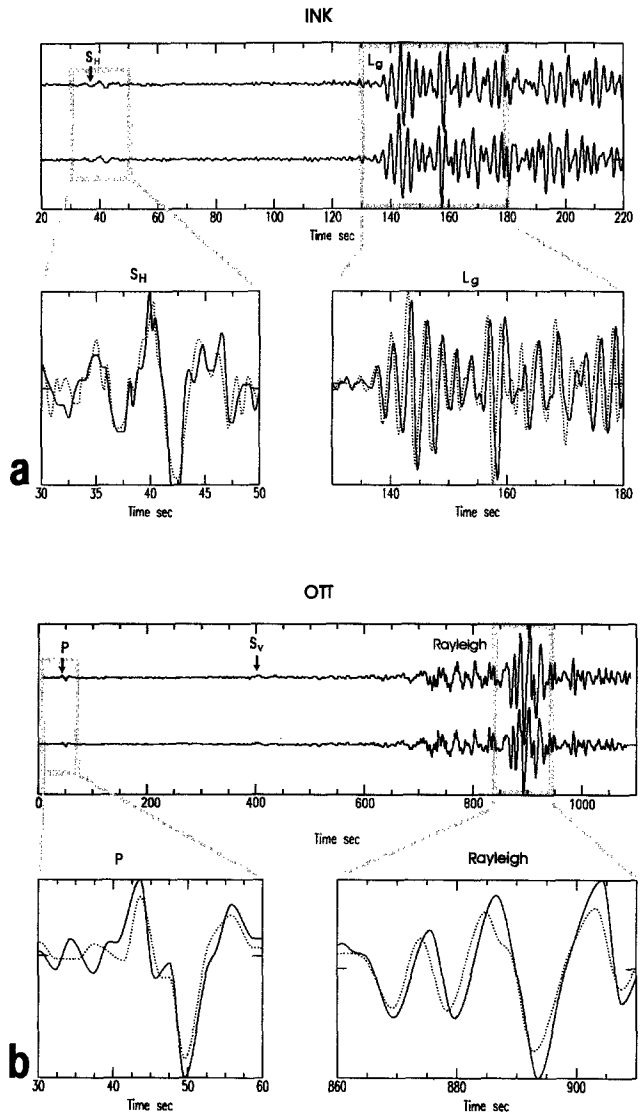

Figure 4. Waveform comparison for the 2 June (solid lines) and 25 July (dotted lines) earthquakes. (a) Short-period E–W seismograms at Inuvik (INK), located to the north of the earthquakes. The traces have been aligned on the *SH* waveform (inset, left). Here, the *Lg* wave train (inset, right) for the July event arrives 0.3 to 0.5 sec early relative to that of the June event, indicating that the July epicenter is 3 to 5 km to the north of the June epicenter. (b) Long-period vertical seismograms at Ottawa (OTT), located to the east of the earthquakes. Aligning the traces on the *P* wave (inset, left) indicates that the Rayleigh wave of the July earthquake arrives 0.8 to 1.2 sec early (inset, right) relative to that of the June event. This requires the July epicenter to be 4 to 6 km to the east of the June epicenter.

body waves (described later in this article) and, for the June event, from the aftershock data. For the June event, the focal depth determined from modeling long-period *P* waveforms is 15.0 ± 2 km, and the best depth from the short-period *P* waveforms is 15.5 ± 2 km. This suggests that the initial rupture was slightly deeper than the centroid location. For the July event, the depth is estimated at 16.0 ± 2 km from the long-period waves, and 16.5 ± 2 km from the short-period waveforms. The relative depths of these two events can be accurately constrained by comparing waveforms. In Figure 5, stacked *P* waveforms for the two earthquakes are compared. Each stack is composed of eight *P* waveforms at stations in eastern and southeastern North America. Note that for the July event, the depth phases *pP* and *sP* arrive 0.2 and 0.3 sec later, respectively, than the direct *P* wave, requiring the July earthquake to be 1 km deeper than the June event. These depth estimates are in good agreement with the mean focal depth of 17.5 ± 2 km for the most precisely located aftershocks (see the following section).

Aftershock Study

Both the 2 June and 25 July 1978 earthquakes were followed by aftershock sequences. Over a 2-week period immediately following the June earthquake, 52 aftershocks of $M_L \geqq 0.9$ were recorded at Port Hardy (PHC), the closest permanent seismic station (70 km from the epicenter). The aftershock sequence for the July earthquake had a very similar decay pattern in time (see Spindler, 1991), but only 26 $M_L \geqq 0.9$ aftershocks were recorded at PHC in the 2 weeks following this earthquake. The *S-P* times for the July aftershocks recorded at PHC (north of the epicenter) range from 7.7 to 8.2 sec, compared to 8.2 to 8.6 for the June aftershocks recorded at this station. This suggests that the aftershock

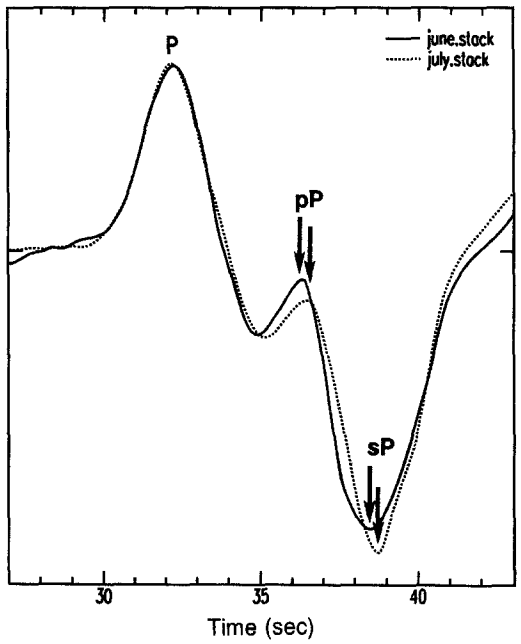

Figure 5. Comparison of the *P* waveforms for the 2 June and 25 July earthquakes. Each trace represents the stack of eight *P* waves at stations in North America. The depth phases *pP* and *sP* arrive later for the July earthquake relative to the June event, indicating a focal depth 1 km deeper for the former.

areas are adjacent, with the July activity being concentrated a few kilometers to the north of the June sequence.

Portable Array. An array of four short-period vertical-component analog seismograph stations was deployed in the vicinity of the Brooks Peninsula following the 2 June mainshock (Fig. 6) and operated for a 4-day period (9 to 12 June 1978). During that time, 42 locatable aftershocks were detected. Their magnitudes ranged between M_L − 0.3 and M_L 3.7. The array surrounded the aftershock area, providing good horizontal and vertical control for local hypocentral solutions.

The hypocenters were determined using hypoellipse (Lahr, 1980) and a local earth model derived from the refraction model developed by McMechan and Spence (1983). Details of this analysis are given by Spindler (1991). Of the 42 aftershocks detected by the temporary array, 18 are considered to be most accurately located. These events were located using a minimum of six impulsive arrivals, including at least two *S* phases. The uncertainties (one standard deviation) were in all cases less than 1.5 km in both the horizontal and vertical directions, with an average horizontal uncertainty of ±0.7 km and an average depth uncertainty of ±1.0 km. These more precisely located events (black dots in Fig. 6) were used to obtain the nominal hypocenter for the June mainshock and to estimate the rupture surface.

The aftershocks form a circular area of ~9 km diameter, centered on 50.15° N, 127.84° W. We assign this location as the epicenter for the 2 June mainshock (with uncertainties of ±3.5 km for both the latitude and the longitude). This average location is robust; it is obtained using all 18 of the most accurately located aftershocks and using only the 13 largest ($M_L > 0.5$) best-located aftershocks. Note that within this aftershock distribution, there is a region (just to the west of the chosen epicenter) in which no aftershocks were located (Figs. 6 and 7). If this void is real, it may represent the surface projection of the mainshock rupture surface. It is about the correct size (see later calculation of the size of the rupture surface). Also note in Figure 6 that the waveform comparison places the July mainshock 5 to 7 km to the northeast of the June mainshock, just at the edge of the June aftershock distribution.

An attempt was made to determine the orientation of the fault plane by plotting cross sections from the 18 most accurately located aftershocks (Fig. 7). The N–S and E–W cross sections were chosen to align with the well-constrained nodal planes determined for the June mainshock (see next section). Although there is no clearly discernable fault plane in the aftershock data, we argue for rupture on a shallow-dipping E–W plane rather than a near-vertical N–S fault, based on four observations:

1. The best-located aftershocks are tightly clustered in depth—within uncertainties 88% of the aftershocks lie between 16 and 19 km depth—and are consistent with a nodal plane dipping 25° to the north (Fig. 7). For rupture on a near-vertical fault, a more pronounced aftershock distribution would be expected in the vertical plane, as rupture would likely propagate toward the surface.
2. The best-located aftershocks span a region of 4 km in length in a N–S direction (Fig. 7) and 7 km in length in an E–W direction. If rupture had occurred on a N–S-striking near-vertical fault, one would expect the opposite pattern—with aftershocks most tightly clustered in the E–W direction. As illustrated in the E–W cross section in Figure 7, this is clearly not the case (note that the width of the shaded bar denotes the average horizontal uncertainty of ±0.7 km for the epicenters).
3. The NE–SW separation of the June and July mainshocks (Fig. 6) and the slightly deeper hypocenter of the July event are both consistent with rupture on a near-horizontal plane dipping to the north but are not consistent with rupture on a near-vertical N–S-striking fault.
4. If the void in the aftershock pattern (Fig. 6) represents the mainshock rupture area, this would require rupture on a near-horizontal plane, as such a pattern would not be

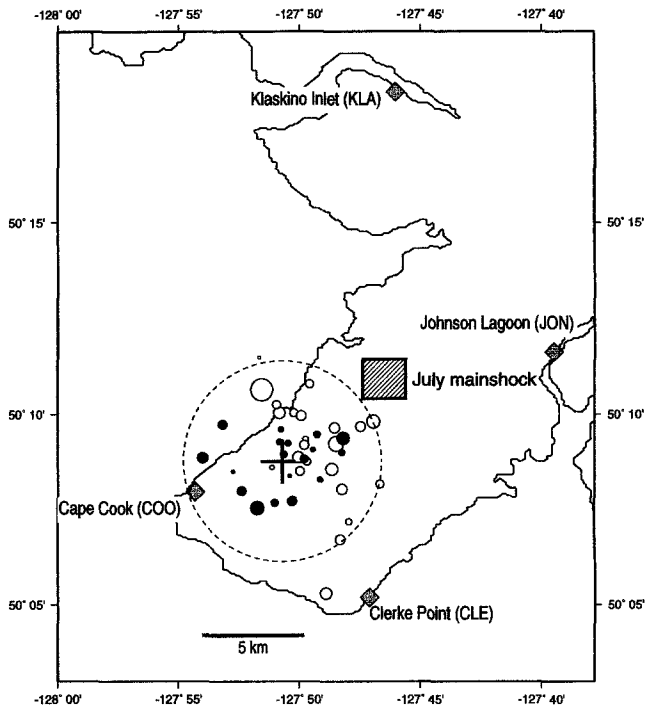

Figure 6. Locations of the aftershocks of the 2 June earthquake located using data from a temporary seismograph array (filled diamonds). The best-located aftershocks (using a minimum of six impulsive phases, including at least 2 *S* phases, and with horizontal and depth uncertainty <1.5 km) are indicated by solid dots. Open dots denote those less well-constrained aftershocks. The cross represents the average location of the best-located aftershocks. This is assigned as the mainshock location for the 2 June earthquake. All but one of the 42 aftershocks are located within a 4.5-km radius of this location. The July mainshock (hatched region) is located near the NE limit of the June aftershock distribution.

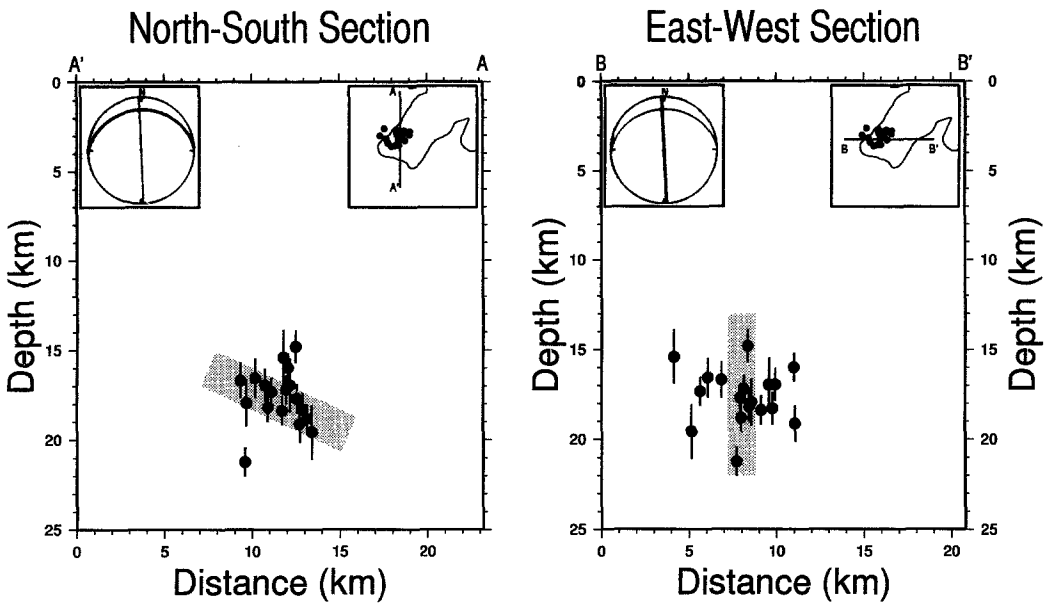

Figure 7. N–S and E–W cross sections of the best-located aftershocks (see inset, right). These projections were chosen based on the well-constrained nodal planes (inset, left) for this earthquake. 90% of the aftershocks are between 16 and 19 km depth, and span 4 km in the N–S direction and 7 km in the E–W direction. Error bars are shown for the focal depths. The shaded band on the N–S cross section represents the nodal plane that dips 25° to the north. The width of the shaded band represents the average depth uncertainty of ±1.0 km. The shaded band on the E–W cross section represents the near-vertical nodal plane, and its thickness represents the average horizontal uncertainty of ±0.7 km.

observed for a near-vertical fault. Although the apparent "void" is not well defined due to the relatively small number of aftershocks, we note that the size of the void corresponds to the rupture surface area that we calculate based on the stress drop.

Focal Mechanisms

Focal mechanisms were determined by using first-motion polarities and by modeling teleseismic and regional body waves. Estimates of the mechanisms based on an analysis of surface waves (Spindler, 1991) are nearly identical to those of the first-motion study, described below, but provide no additional constraints.

First-Motion Polarities. Focal mechanisms were determined for the mainshocks using first-motion polarities. The data were a mixture of long- and short-period readings, along with polarities obtained from the International Seismological Centre (ISC) bulletin. For the 2 June event, a total of 115 polarities were used: 66 read by the authors (27 long period and 39 short period) and 49 first motions taken from the ISC bulletin. For the July event, a total of 78 first-motions were used: 34 read by the authors (30 long period and 4 short period) and 44 from the ISC bulletin. These data were used with the program PNODAL (Wickens and Hodgson, 1965) to compute the first-motion focal mechanisms.

The solutions for the June and July events were very similar (Fig. 8). A best-fitting composite focal mechanism constructed from the aftershock first-motion data (Fig. 8) is almost identical to that of the June mainshock. The pattern of first motions clearly allows us to rule out a pure-thrust mechanism (i.e., a megathrust earthquake on a shallow northeast-dipping plane). In all cases, there is a well-constrained near-vertical nodal plane striking N–S and a shallow north-dipping ENE-striking nodal plane. The latter is not well defined by the data; the dip angle of this plane may range from 0° to 40°. Based on the first-motion data alone, one cannot rule out a shallow (0° to 30°) south-dipping ENE striking nodal plane.

These solutions indicate either nearly pure left-lateral strike-slip motion on a shallow-dipping (0° to 40°) ENE-striking fault (the preferred solution) or near-vertical motion (east side down) on a north-striking, steeply dipping (75° to 85° E) plane.

Body-Wave Modeling. Forward modeling of regional and teleseismic *P* waveforms was employed to further constrain the source mechanism estimated from the first-motion analysis and to provide an estimate of the focal depth, source-time function, and seismic moment for each earthquake. The technique of Langston and Helmberger (1975) was used. A simple layer-over-a-half-space model (32-km thick crust, with an average crustal velocity of 6.2 km/sec) was used to generate the synthetics, and a Futterman (1962) operator, t^*,

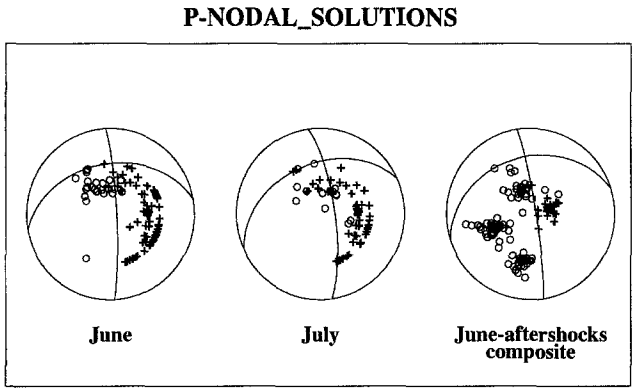

Figure 8. *P*-nodal solutions (lower-hemisphere projection) for the 2 June and 25 July earthquakes and a composite solution for the June aftershocks. Crosses denote compressions, and circles indicate dilatations. In each case, the N–S-striking nodal plane is well constrained by the data, the shallow-dipping E–W-striking nodal is not as well constrained, with a range of dip angles from 0° to 40°.

of 1.0 sec, was applied for anelastic attenuation. In all cases, the waveforms modeled were from stations of the World-Wide Standard Seismograph Network (WWSSN) or of the Canadian Standard Seismograph Network (having a very similar instrument response to WWSSN stations).

For the June earthquake, a total of 17 long-period *P* waves, and 6 short-period *P* waves (Table 2) covering a wide azimuthal range were modeled. The best fit to the waveforms was provided by a triangular source-time function of 2.4-sec total duration for the long-period waveforms, and 0.4-sec total duration for the short-period waveforms. Initially, synthetic seismograms were generated using the *P*-nodal solution. These provided a good fit to the observed waveforms, with the exception of those stations closest to the nodal planes (particularly COL, INK, MBC, and PTO). An improved fit to these waveforms, and a comparable fit to all other waveforms (Fig. 9), was provided by our preferred mechanism: strike (θ) = 267°, dip (δ) = 25°, and slip (ϕ) = 0°. This represents either pure left-lateral slip along an E–W-striking plane dipping at 25° to the north, or predominantly down drop (east-side down) on a vertical, N–S-striking fault. Note that the strike and dip of the N–S-trending nodal plane are very well constrained by stations INK and MBC, and the dip of the E–W-striking nodal plane is well constrained by stations INK and COL. An uncertainty of ±5° is estimated for each of these parameters. The depth phases *pP* and *sP* are clearly observed in both the long-period and short-period waveforms (Fig. 5) and provide depth estimates of 15.0 ± 2 and 15.5 ± 2 km, respectively. The simplicity of the short-period waveforms (Fig. 9) rules out source complexity (multiple events). A seismic moment of (1.8 ± 0.4) × 10^{24} dyne-cm was estimated from the long-period *P* waves, and (0.6 ± 0.4) × 10^{24} dyne-cm was estimated from the short-period waveforms.

Table 2
Body-Wave Data Modeled

Station	Azimuth (deg)	Distance (deg)	Component
AAM	87	31	**LPZ**
ANP	301	83	LPZ
BLA	93	36	**LPZ**
COL	332	18	**LPZ**
EPT	131	24	**LPZ**
FCC	53	21	**LPZ**
FFC	64	16	**LPZ**
FRB	43	33	**LPZ,SPZ**
FVM†	100	29	LPZ
GOL	115	19	**LPZ**
GSC	147	17	**LPZ**
INK	353	18	**LPZ**
LHC*	79	25	LPZ
LUB*	121	25	LPZ
MAT	298	65	SPZ
MBC	5	26	LPZ
OGD	83	38	LPZ*, **SPZ**
OTT	77	35	**LPZ**
PTO	43	75	LPZ
RES	18	28	SPZ
SHA	108	35	**LPZ**
SHK	300	70	**SPZ**
TOL	41	78	**SPZ**

Boldface denotes stations/components modeled for both earthquakes. Regular font denotes stations/components modeled for the June event only.
*Denotes stations/components modeled for the July event only.

For the July event, a total of 17 long-period and 4 short-period *P* waveforms were modeled (Table 2). Both the amplitude and the shape of the waveforms were identical, with few exceptions, to those of the June earthquake (Fig. 10). The only waveforms that differ from those of the June event are the long-period *P* waves at COL and INK. At these stations, the amplitude of the direct *P* wave is clearly smaller, relative to the depth phases *pP* and *sP*, for the July waveforms relative to the June waveforms (compare Figs. 9 and 10). This waveform difference could not be satisfied by changing the strike or dip of the N–S nodal plane but only by changing the dip of the E–W-striking nodal plane. Increasing the dip of this plane from 25° (June event) to 40° provided a very good fit to COL, INK, and all other waveforms, both short period and long period (Fig. 10). The degree to which the long-period *P* waveform at COL and INK varies with the dip angle of the E–W-trending nodal plane, as illustrated in Figure 11. Thus, the mechanism of the July event from body-wave modeling (θ = 267°, δ = 40°, ϕ = 0°) is identical to that of the June event, with the exception of a more steeply dipping, E–W-striking nodal plane. The focal depth of the July event is also well constrained from the body waves to be 16.0 ± 2 km (long period) and 16.5 ± 2 km (short period). As described earlier, the relative depth difference between the June and July events is clearly observable and well constrained from the *P* waveforms (Fig. 5). The source-time function for this earthquake is identical

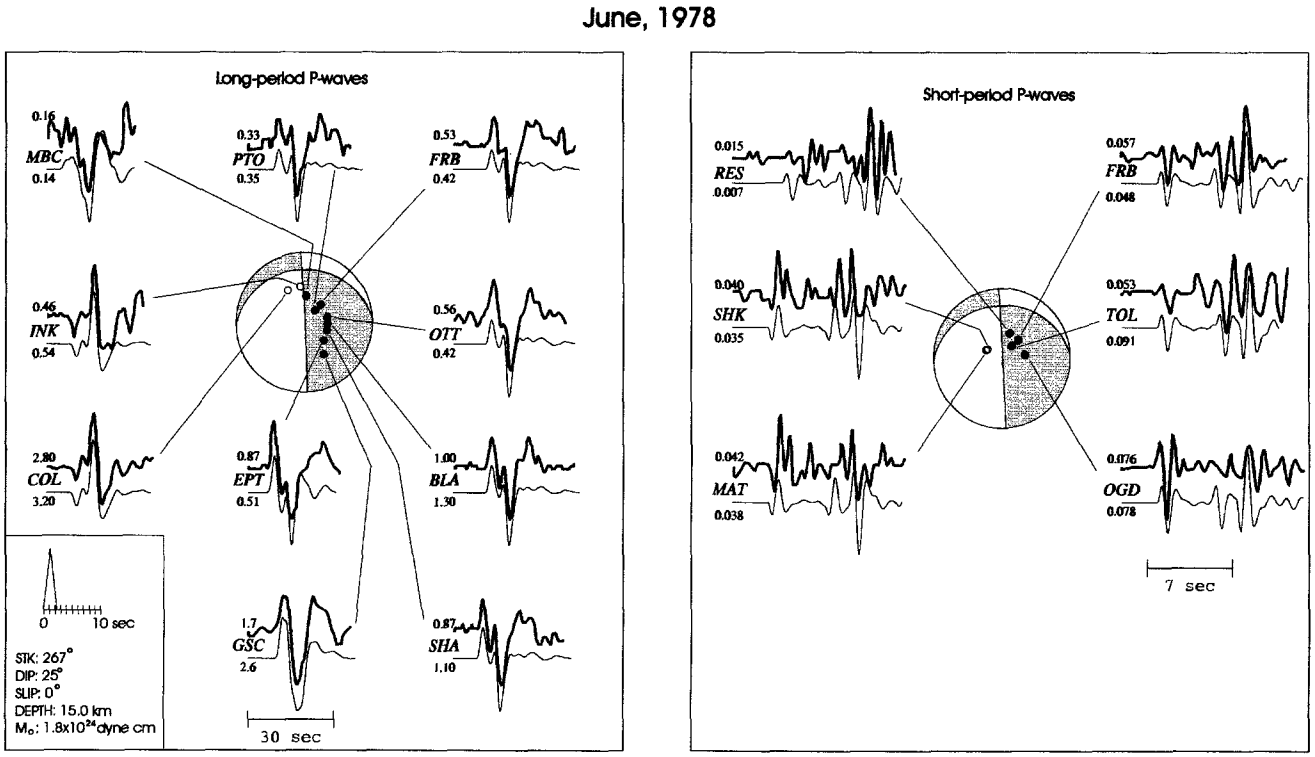

Figure 9. Body-wave modeling results for the June earthquake. The derived focal mechanism is shown with the observed (top traces) and synthetic (bottom traces) teleseismic and regional *P* waveforms. Long-period data are shown on the left, and short-period data are on the right. Amplitudes, corrected for instrument gain, are in units of 10^{-3} cm. The seismic moment is calculated at 1.8×10^{24} dyne-cm and the source duration at 2.4 sec.

to that of the June event, and the seismic moment estimates were identical, within uncertainties [$(1.7 \pm 0.4) \times 10^{24}$ dyne-cm from the long-period *P* waves and $(0.8 \pm 0.4) \times 10^{24}$ dyne-cm from the short-period waveforms].

Magnitudes, Seismic Moments, Stress Drops, and Rupture Surface

The ISC calculated m_b values of 5.1 and 5.0 and M_S values of 5.2 and 5.1 for the June and July events, respectively. To more effectively compare the size of the two earthquakes, we calculated M_S values with a common suite of 13 stations. We used only the ISC data in the 18- to 22-sec period range and scaled data from long-period seismograms in the Canadian seismograph network. The June and July events were found to have surface-wave magnitudes of 5.21 and 5.16, again suggesting that the June earthquake was slightly larger. This is consistent with seismic moments calculated from the long-period body-wave data in the previous section [$(1.8 \pm 0.4) \times 10^{24}$ dyne cm for the June event and $(1.7 \pm 0.4) \times 10^{24}$ dyne cm for the July event], which also suggest that the first earthquake was slightly larger. These moment values both yield a moment magnitude of $M_W = 5.5$.

Stress drops were calculated from far-field displacement spectra, using the method of Brune (1970, 1971). The data were obtained from the four digital stations (ALB, PIB, PGC, and HYC) that were operating at the time (Fig. 3 inset). Both events showed average stress drops of 16 bars (see Spindler, 1991, for details). Stress drops were also estimated using empirical relationships. The source duration–seismic moment relationship of Cohn *et al.* (1982) yields a stress drop of 20 bars for the June event and 18 bars for the July event, and extrapolating the M_S–M_0 relationship of Kanamori and Anderson (1975) yields a stress drop of 17 bars for each of these events (based on $M_S = 5.2$). The relatively low stress drop indicates that the earthquakes did not occur on new or well-cemented, older fractures.

The sizes of the rupture surfaces were estimated from the stress drop, using the seismic moment determined from the body-wave data and Brune's relation (Brune, 1970, 1971). The rupture surfaces were found to be 3.4 to 3.7 km and 3.4 to 3.6 km in radius for June and July, respectively. The radius of the rupture surface, as estimated from the aftershock distribution, was between about 3.0 km (region of no aftershocks) and 4.5 km (maximum aftershock extent), which is consistent with the value obtained from the stress drop.

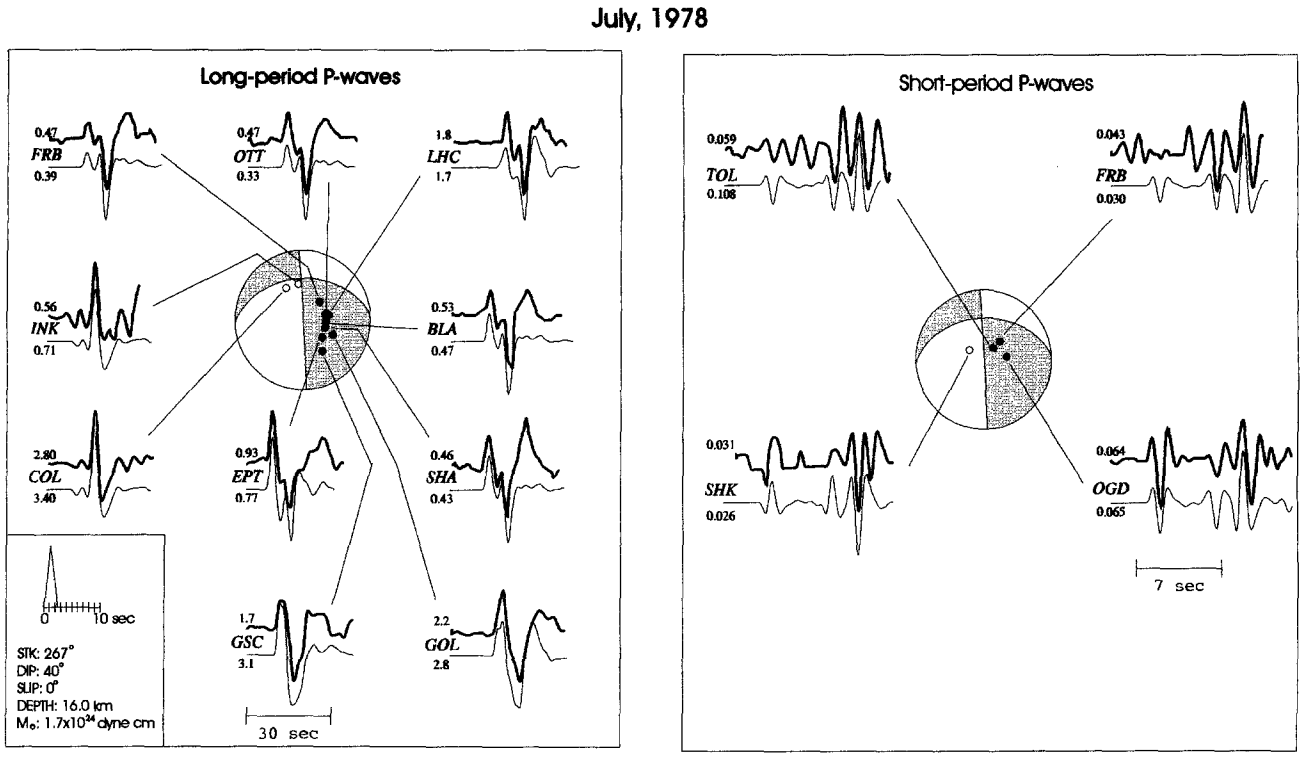

Figure 10. Body-wave modeling results for the July earthquake, as described in Figure 9. The seismic moment is calculated at 1.7 × 10^{24} dyne-cm and the source duration at 2.4 sec.

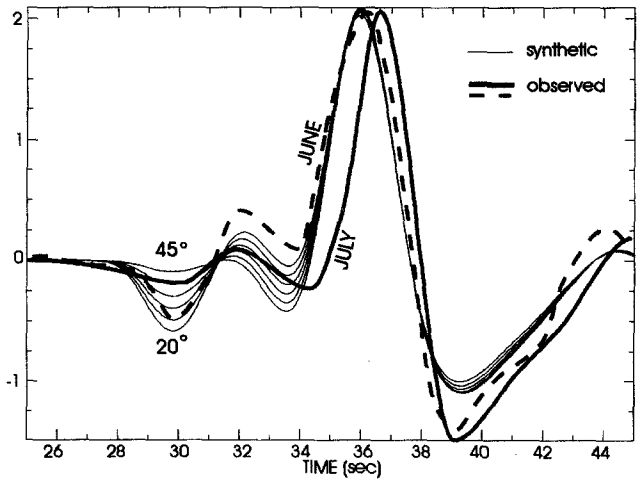

Figure 11. Resolution of the dip angle of the E–W-striking nodal plane. The observed *P* waveforms recorded at COL for the June and July events (heavy dotted and solid lines, respectively) are compared to synthetic waveforms (thin lines) generated using dip angles ranging from 20° to 45°. Changing the dip angle makes a significant difference in the amplitude of the first trough relative to the second, with the June waveform requiring a dip angle of 25° and the July waveform requiring a dip angle of 40°.

Discussion

Summary

The 2 June and 25 July 1978 Brooks Peninsula earthquakes were essentially identical events that occurred within the North American plate at a depth of 15 to 17 km, approximately 5 to 10 km above the subducting oceanic plate (Fig. 12). The surface-wave magnitudes, seismic moments, and stress drops showed both events to be of similar size. However, there was a difference in the aftershocks, in that the aftershock sequence of the July event (26 aftershocks of $M_L \geqq 0.9$ recorded within 2 weeks of the mainshock) was smaller than that of the June earthquake (52 aftershocks of $M_L \geq 0.9$ recorded within 2 weeks of the mainshock). The well-located aftershocks of the June event, recorded by a local temporary seismic array, define a circular region of ~9 km in diameter, centered on 50.15° N, 127.84° W. We chose this location as the epicenter of the 2 June mainshock. By comparing the seismic waveforms of these two events made at stations covering a range of azimuth, we obtain excellent constraints on the relative location and depths of these two earthquakes: the July epicenter was located 4 to 7 km to the NE of the June event, and 1 km deeper.

The focal mechanisms obtained from first-motion patterns and body-wave modeling were nearly identical. Both showed nearly pure left-lateral strike-slip motion on shallow north-dipping ENE-striking fault, or mainly vertical motion (east-side down) along a steeply dipping N–S-striking fault. Based on both the aftershock pattern that shows a near-circular rupture in a horizontal plane, and the relative locations, we prefer the north-dipping ENE plane as the best faulting model. The body-wave modeling requires that the dip angle of the ENE-striking fault increase from 25° for the June event to 40° for the slightly deeper July earthquake. This indicates fault segmentation and suggests why there were two $M_W = 5.5$ earthquakes rather than a single $M_W = 5.7$ event. The pressure axes of the June and July earthquakes have azimuths of 234° and 244°, respectively, and plunges of 40° and 33°.

Tectonic Implications

The focal mechanism and depth of these two earthquakes indicates that they were not megathrust events on the

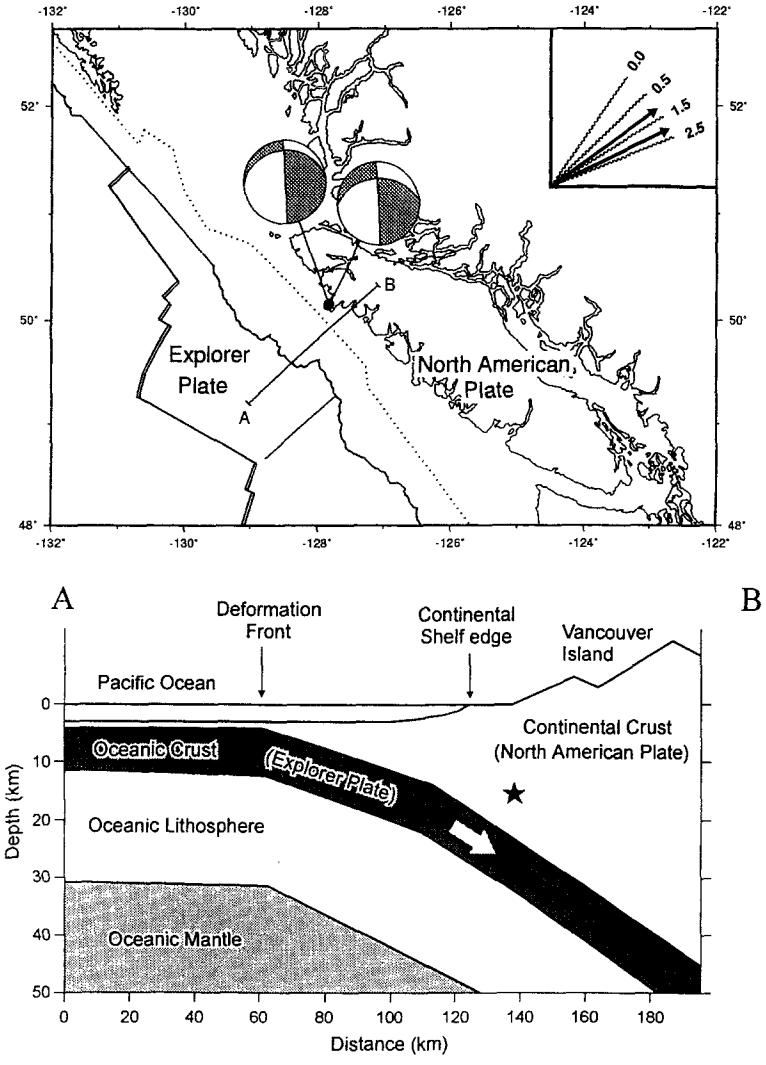

Figure 12. (a) Locations and focal mechanisms of the 1978 Brooks Peninsula earthquakes. The thin solid line to the west of Vancouver Island denotes the deformation front; the dotted line represents the edge of the continental shelf. The line A-B denotes the location of the cross section (below). The inset shows the orientation of the pressure axes for these two earthquakes (thick arrows); thinner lines denote the direction of interaction (at the Brooks Peninsula) of the Explorer plate (EXP) relative to the North America plate (NAM) at times of 2.5 m.y., 1.5 m.y., and 0.5 m.y. (from Riddihough, 1984). The 0.0 m.y. direction was obtained by extrapolating the EXP/NAM pole position to the present time, and is subject to significant uncertainty. The consistency between the pressure axes for the 1978 Brooks Peninsula earthquakes and the EXP–NAM interaction directions suggest coupling of the Explorer and North American plates along this portion of the convergent margin. (b) Cross section along the line A-B in the vicinity of the Brooks Peninsula region showing that the 1978 Brooks Peninsula earthquakes (star) occurred within the North American crust, 5 to 10 km above the top of the subducting oceanic plate. The depth to the Explorer plate is based on nearby seismic reflection studies (see Fig. 1).

Explorer–North America plate boundary, but rather that they occurred within the North American plate, 5 to 10 km above the megathrust.

Thus, these earthquakes provide key information for understanding the complex tectonics in the region of microplates at the northern end of the Cascadia subduction zone because they reveal the orientation of tectonic stress within the North American plate in the region of the Brooks Peninsula. The orientation of the pressure axes deduced from the focal mechanisms is consistent with northeast–southwest compression. This is the approximate orientation of the relative motion between the Explorer (EXP) and North American (NAM) plates (Fig. 12) if the contemporary interaction vector is extrapolated from the model of Riddihough (1984). The agreement between the earthquake pressure axes and the EXP–NAM interaction direction suggests that the rigid-plate modeling of Riddihough (1984) is effective in predicting the contemporary stress regime, and it implies coupling on the subduction boundary in the region of the Brooks Peninsula. The relatively low stress drops of these two earthquakes (less than 20 bars) is consistent with low coupling stress deduced for the Juan de Fuca portion of the Cascadia subduction margin south of the Nootka Fault (Wang *et al.*, 1995).

Conclusions

Two earthquakes of M_W 5.5 occurred beneath the northwestern shore of the Brooks Peninsula on 2 June and 25 July 1978. The deployment of a temporary seismograph array after the first earthquake allowed the aftershocks of this event to be well located. Based on the aftershock distribution, the 2 June earthquake was located at 50.15° N, 127.84° W. The July epicenter was calculated to be 4 to 7 km to the NE of this location. Well-constrained focal mechanisms were determined using first-motion and body-wave modeling. The mechanisms are essentially identical; the preferred fault plane displayed left-lateral strike-slip motion along an E–W-striking fault, dipping at 25° to the north for the June event and 40° to the north for the July event. The relative locations and focal mechanisms suggest that these are adjacent events on a common, although segmented, fault. The focal depths, based on body-wave modeling, are 15.0 and 16.0 km, respectively. This places this earthquakes in the crust of the North American plate, 5 to 10 km above the top of the downgoing Explorer plate. The focal mechanisms and depth for these earthquakes rules out their being megathrust earthquakes on the Explorer–North American plate interface.

The focal mechanisms of these earthquakes are not consistent with the mapped surface faults near the Brooks Peninsula; however, the orientation of the pressure axes is consistent with the expected convergence between the Explorer and North American plates. We suggest that these earthquakes reflect coupling between the downgoing and overlying plates across the convergent margin at the northern end of the Cascadia subduction zone. The low stress drop of these events (less than 20 bars) is consistent with low coupling stress across the Cascadia subduction zone fault.

Acknowledgments

We gratefully acknowledge thorough reviews of this manuscript by Bob Crosson, Allison Bent, and an anonymous reviewer. Many of the diagrams in this manuscript were generated using Generic Mapping Tool (Wessel and Smith, 1991). Geological Survey of Canada Contribution Number 1996241.

References

Atwater, B. *et al.* (1995). Summary of coastal geologic evidence for past great earthquakes at the Cascadia subduction zone, *Earthquake Spectra* **11,** 1–18.

Botros, M., and H. P. Johnson (1988). Tectonic evolution of the Explorer—northern Juan de Fuca region from 8 Ma to the present, *J. Geophys. Res.* **93,** 10421–10437.

Brune, J. N. (1970). Tectonic stress and the spectra of seismic shear waves from earthquakes, *J. Geophys. Res.* **75,** 4997–5009.

Brune, J. N. (1971). Correction, *J. Geophys. Res.* **76,** 5002.

Cande, S. C. and R. B. Leslie (1986). Late Cenozoic tectonics of the southern Chile trench, *J. Geophys. Res.* **91,** 471–497.

Clowes, R. M., D. J. Baird, and S. A. Dehler (1997). Crustal structure of the Cascadia subduction zone, southwestern British Columbia, from potential field and seismic studies, *Can. J. Earth Sci.* (in press).

Cohn, S. N., T.-L. Hong, and D. V. Helmberger (1982). The Oroville earthquakes: a study of source characteristics and site effects, *J. Geophys. Res.* **87,** 4585–4594.

Davis, E. E. and R. G. Currie (1993). Geophysical observations of the northern Juan de Fuca Ridge system: lessons in sea-floor spreading, *Can. J. Earth Sci.* **30,** 278–300.

Davis, E. E. and R. P. Riddihough (1982). The Winona basin: structure and tectonics, *Can. J. Earth Sci.* **19,** 767–788.

Ellis, R. M., J. F. Cassidy, and G. C. Rogers (1996). The shear-wave velocity structure beneath northern Vancouver Island, British Columbia (abstract), *Seism. Res. Lett.* **67,** 37.

Forsythe, R. and E. Nelson (1985). Geological manifestations of ridge collision: evidence from the Golfo de Penas-Taito Basin, southern Chile, *Tectonics* **4,** 477–495.

Futtermann, W. I. (1962). Dispersive body waves, *J. Geophys. Res.* **67,** 5279–5291.

Horner, R. B., A. E. Stevens, and R. J. Wetmiller (1979). Canadian earthquakes—1978, *Seism. Ser. Earth Physics Branch, Ottawa,* No. 83, 53 pp.

Kanamori, H. and D. L. Anderson (1975). Theoretical basis of some empirical relations in seismology, *Bull. Seism. Soc. Am.* **65,** 1073–1095.

Lahr, J. C. (1980). Hypoellipse/VAX: a computer program for determining local earthquake hypocentral parameters, magnitude and first motion pattern, *U.S. Geol. Surv. Open-File Rept. 80-59,* 67 pp.

Langston, C. A. and D. V. Helmberger (1975). A procedure for modelling shallow dislocation sources, *Geophys. J. R. Astr. Soc.* **42,** 117–130.

Lewis, T. J., C. Lowe, and T. S. Hamilton (1997). The continental signature of a ridge-trench-transform triple junction: Northern Vancouver Island, *J. Geophys. Res.* **102,** 7767–7781.

McMechan, G. A. and G. S. Spence (1983). P-wave velocity structure of the Earth's crust beneath Vancouver Island, *Can. J. Earth Sci.* **20,** 742–752.

Muller, J. E., K. E. Northcote, and D. Carlisle (1974). Geology and mineral deposits of Alert-Cape Scott map area, Vancouver Island, British Columbia, Canada, *Geol. Surv. Canada Pap. 74-8.*

Oppenheimer, D. *et al.* (1993). The Cape Mendocino, California, earthquakes of April 1992: subduction at the triple junction, *Science* **261,** 433–438.

Riddihough, R. P. (1977). A model for recent plate interactions off Canada's west coast, *Can. J. Earth Sci.* **14,** 384–386.

Riddihough, R. P. (1984). Recent movements of the Juan de Fuca plate system, *J. Geophys. Res.* **89,** 6980–6994.

Riddihough, R. P. and R. D. Hyndman (1991). Modern plate tectonic regime of the continental margin of western Canada, in *The Cordilleran Orogen: Canada,* H. Gabrielse and C. J. Yorath (Editors), Geological Survey of Canada, Geology of Canada (DNAG), Vol. 4, pp. 435–455.

Rogers, G. C. (1988). An assessment of the megathrust earthquake potential of the Cascadia subduction zone, *Can. J. Earth Sci.* **25,** 844–852.

Smith, S. W., J. S. Knapp, and R. S. McPherson (1993). Seismicity of the Gorda plate, structure of the continental margin, and an eastward jump of the Mendocino triple junction, *J. Geophys. Res.* **98,** 8153–8171.

Smyth, W. R. (1985). Geology of the Brooks Peninsula, Vancouver Island, *Ministry of Energy, Mines, and Petroleum Resources, B.C. Paper 1985-1,* 161–169.

Spindler, C. L. P. (1991). Analysis of the 1978 Brooks Peninsula, Vancouver Island earthquakes, *M.Sc. Thesis,* University of Victoria, Victoria, British Columbia.

Tinker, M. A. and S. L. Beck (1995). Inversion of regional surface-wave spectra for source parameters of aftershocks from the 1992 Petrolia earthquake sequence, *Bull. Seism. Soc. Am.* **85,** 705–715.

Velasco, A. A., C. J. Ammon, and T. Lay (1994). Recent large earthquakes near Cape Mendocino and in the Gorda plate: broadband source time functions, fault orientations, and rupture complexities, *J. Geophys. Res.* **99,** 711–728.

Wang, K., and G. C. Rogers (1994). An explanation for the double seismic layers north of the Mendicino triple junction, *Geophys. Res. Lett.* **21,** 121–124.

Wang, K., T. Mulder, G. C. Rogers, and R. D. Hyndman (1995). Case for very low coupling stress on the Cascadia subduction fault, *J. Geophys. Res.* **100,** 12907–12918.

Weichert, D. W. and J. C. Newton (1970). Epicentre determination from first arrival times at Canadian stations, *Seism. Ser. Earth Physics Branch, Ottawa,* No. 59, 16 pp.

Wessel, P. and W. H. F. Smith (1991). Free software helps map and display data, *EOS* **72,** 445–446.

Wickens, A. J. and J. H. Hodgson (1965). Computer reeavaluation of earthquake mechanism solutions, *Publications of the Dominion Observatory, Ottawa,* **16,** No. 10, 1–560.

Wilson, D. S. (1988). Tectonic history of the Juan de Fuca ridge over the last 40 million years, *J. Geophys. Res.* **93,** 11863–11876.

Geological Survey of Canada
Pacific Geoscience Centre
P.O. Box 6000
Sidney, British Columbia V8L 4B2
(C. S., G. C. R., J. F. C.)

Department of Physics and Astronomy
University of Victoria, P.O. Box 1700
Victoria, British Columbia V8W 2Y2
(C. S., G. C. R.)

Manuscript received 27 August 1996.